Geophysical Journal International

Geophys. J. Int. (2013) **195,** 532–543
Advance Access publication 2013 July 10

doi: 10.1093/gji/ggt236

Scattering of *SH* waves by a circular sectorial canyon

Kao-Hao Chang,[1] Deng-How Tsaur[2] and Jeen-Hwa Wang[1]

[1] *Institute of Earth Sciences, Academia Sinica, Nangang, Taipei* 11529*, Taiwan, R.O.C. E-mail: khchang@earth.sinica.edu.tw*
[2] *Department of Harbor and River Engineering, National Taiwan Ocean University, Jhongjheng District, Keelung* 20224*, Taiwan, R.O.C.*

Accepted 2013 June 14. Received 2013 May 9; in original form 2012 November 8

SUMMARY

The scattering of plane *SH* waves incident on a circular sectorial canyon is considered. An accurate region-matching technique is applied to derive a rigorous series solution. Appropriate wavefunctions are employed to describe antiplane motions. Judicious basis functions, involving Gegenbauer polynomials, are well utilized to correctly capture the singular behaviour in stress fields near the canyon bottom. The enforcement of matching conditions on the auxiliary boundary leads to the determination of unknown coefficients. Plotted results demonstrate the influence of pertinent parameters on surface and subsurface motions. Both steady-state and transient results are included. The solution technique proposed achieves a considerable reduction in the computational effort, facilitating benchmark computations. The derived series solution enriches the limited list of series solutions presently known for canyon problems related to *SH*-wave scattering.

Key words: Earthquake ground motions; Theoretical seismology; Wave scattering and diffraction; Wave propagation.

1 INTRODUCTION

Rugged topographic relief has been well known as one of the leading factors substantially affecting the spatial and temporal variations in seismic ground motions (e.g. Boore 1973; Bouchon 1973; Spudich *et al.* 1996). The near-surface complexity in local geometric discontinuities (e.g. canyons, ridges, slopes and cliffs) intensifies the great diversity of seismic wavefields. This is usually called the *topographic effect* in the pertinent literature (e.g. Geli *et al.* 1988; Kawase & Aki 1990; Hartzell *et al.* 1994; Scott *et al.* 1997). Over the years, the measurement, assessment and prediction on the potential topographic amplification during earthquake shaking (e.g. Davis & West 1973; Celebi 1987; Hough *et al.* 2010) have been of continued interest to researchers in shallow geophysics, seismology, civil engineering, etc.

Concave topographies like canyons are one common type of natural landforms on Earth's surface. Since the early 1970s, various conceptual models have been built to approximate the cross-sectional profiles of real canyons. Simply take the *SH*-wave case, for example, two representatives in the range of theoretical concerns are the semi-circular and semi-elliptic canyons (see Trifunac 1973; Wong & Trifunac 1974). Within the range of numerical concerns, simplified models for the triangular, rectangular, trapezoid, cosine-shaped and Gaussian-shaped cases have been devised (see e.g. Aki & Larner 1970; Sánchez-Sesma & Rosenblueth 1979; England *et al.* 1980; Zhou & Chen 2006). Sánchez-Sesma *et al.* (2002) extensively reviewed the analogous models. Indeed, these simplified models have contributed to a qualitative understanding of seismic wave propagation and earthquake-induced motions around canyons.

As to the more complicated terrain, sophisticated numerical schemes are, no doubt, the powerful tools to deal with related issues. In recent decades, the tremendous progress in computer technologies has boosted the growth of numerous mesh discretization techniques. Some of the most popular methods utilized today are the finite-difference, finite-element, spectral-element and boundary-element methods (see e.g. Tessmer *et al.* 1992; Geller & Takeuchi 1998; Komatitsch & Vilotte 1998; Satoh *et al.* 2001; Käser & Dumbser 2006; Kham *et al.* 2006; Ichimura *et al.* 2007; Ma *et al.* 2007; Lee *et al.* 2008; Lombard *et al.* 2008; Lee *et al.* 2009; Kristek *et al.* 2010; Pelties *et al.* 2010). Although these approaches are very flexible for arbitrary surficial configurations, the reliability and accuracy of terminal results from these codes at hand have to be strictly verified with the existing canonical solutions.

For 2-D problems regarding the *SH*-wave scattering in the half-plane, exact analytical solutions, derived by the method of separation of variables (MSV), which is sometimes termed as the method of wavefunction expansions in engineering seismology, are limited to simple geometric shapes. To date, there have only been two cases available, that is, the semi-circular and semi-elliptic canyons (Trifunac 1973; Wong & Trifunac 1974). This is because when the scatterer geometry coincides with any one of the separable coordinate systems, the MSV can be straightforwardly applied to the governing wave equation to yield complete expressions in terms of eigenfunctions (or wavefunctions). However, even for some simple

geometric cases, it is nearly impossible to exactly solve these problems via the MSV. That is to say, the possibility of determining a one-to-one relationship to each unknown coefficient has been excluded. Examples for those whose surface geometries incompletely/completely fitting to a certain separable coordinate system are the truncated semicircular canyons, the partially filled semicircular/semi-elliptic alluvial valleys, the circular-arc mountains and the semi-elliptic hills. Examples for those whose cross-sections, not matching any one of the separable coordinate systems, are the symmetrical V-shaped canyons. Under such a circumstance, if a series solution can be constructed, it may be the best candidate for an exact analytical solution. Recently, a breakthrough in the application of the *region-matching technique* (RMT) to handle aforementioned tasks was made by Chang (2009), Tsaur & Chang (2009), Tsaur (2011) and Tsaur & Hsu (2013). Through the promising RMT, the intrinsic difficulty in utilizing the MSV to derive a chain of series solutions has been conquered.

With regard to the canyons of circular sectorial shapes, there seems to be little attention paid to relevant topics in the literature. Such an idealized shape is approximately close to the cross-section of Pacoima Canyon (see fig. 2b in Wong & Jennings 1975). To the authors' knowledge, the series solution to the scattering problem of circular sectorial canyons is unavailable so far. This has motivated the authors to tackle this issue in a theoretical way. In this work, the RMT is applied to derive a series solution to the case under *SH*-wave excitation.

From a mathematical standpoint, the problem under consideration constitutes an exterior elliptic boundary-value problem involving one salient corner (at the canyon bottom). From fundamental concepts of elastostatics and elastodynamics, it is easy to comprehend that certain quantities such as stress fields may be ill behaved in the vicinity of geometric discontinuities (e.g. corners and sharp edges). The presence of those discontinuous points usually makes the conventional mesh-based methods computationally inefficient (e.g. an enormous amount of discretised meshes required), especially when acquiring an acceptable solution to fields near geometric singularities. When one attempts to get the series solution via the RMT, the exclusion of such significant information may lead to a very large system of equations. Although most results obtained by the RMT may have acceptable accuracy for engineering purpose, further efforts are worthy to be done from the viewpoint of numerical computation for condensing the system of equations and improving the solution accuracy. In view of this, an additional treatment for the corner singularity at the canyon bottom is essential, and it is integrated into the RMT. Such integration is called the accurate RMT hereafter.

The key step of the accurate RMT is to capture the dominant characteristics of stress fields near the canyon bottom. This highlights the importance of blending stress singularities into the solution procedure. At the initial stage, the RMT is followed and subsequently, the present problem is recast in terms of stress integral equations instead of wavefunctions. Therefore, the singular behaviour of stress fields can be incorporated with the RMT in a straightforward way. Meanwhile, the accurate RMT more strongly enhances the overall computational efficiency of solutions than the RMT.

The main contributions of the present work are threefold. First, the proposed series solution is novel since it is likely to be nonexistent in the literature. Second, the canonical geometries studied in the literature are broadened herein to cover a range of circular sectorial shapes. Third, the analytical approach adopted here provides an efficient validation tool for various numerical approximation schemes.

2 THEORETICAL FORMULATIONS

Consider a homogeneous, isotropic, linearly elastic, semi-infinite medium (with shear modulus μ and shear wave velocity c_s) bounded by the horizontal ground surface, inlaid with an infinitely long, circular, sectorial canyon (see Fig. 1). The radius and central angle of the canyon are a and β, respectively. An infinite train of unit-amplitude plane *SH* waves (with angular frequency ω) is incident upon this canyon at an angle α to the y-axis.

As seen in Fig. 1, through introducing a circular-arc auxiliary boundary S_a, the half-plane is divided into two regions, an open region 1 and an enclosed region 2. In these two regions, the steady-state out-of-plane motions are required to satisfy the governing Helmholtz equations, namely

$$\nabla^2 u_j + k^2 u_j = 0, \quad j = 1, 2, \tag{1}$$

where ∇^2 is the 2-D Laplacian and $k = \omega/c_s$ is the shear wavenumber. The subscripts j, where $j = 1$ and 2, denote the total displacement fields in regions 1 and 2, respectively. The time-harmonic factor $\exp(\mathrm{i}\omega t)$ is omitted in all the expressions throughout this paper.

The zero-stress boundary conditions on the horizontal ground surface and the canyon surface are

$$\tau_{\theta z}^{(1)} = \frac{\mu}{r}\frac{\partial u_1(r,\theta)}{\partial \theta} = 0, \quad \text{for} \quad \theta = \pm\frac{\pi}{2} \quad \text{and} \quad r > a, \tag{2}$$

$$\tau_{rz}^{(1)} = \mu\frac{\partial u_1(r,\theta)}{\partial r} = 0, \quad \text{for} \quad -\frac{\pi}{2} < \theta < -\frac{\pi}{2} + \beta \quad \text{and} \quad r = a, \tag{3}$$

$$\tau_{\theta z}^{(2)} = \frac{\mu}{r}\frac{\partial u_2(r,\theta)}{\partial \theta} = 0, \quad \text{for} \quad \theta = -\frac{\pi}{2} + \beta, \frac{\pi}{2} \quad \text{and} \quad r < a. \tag{4}$$

The free-field displacement u^F, existing in the half-plane medium without any surface/subsurface irregularities, can be expressed as a sum of the incident waves and their specularly reflected waves from the horizontal ground surface, that is,

$$u^F(r,\theta) = \exp[\mathrm{i}kr\cos(\theta+\alpha)] + \exp[-\mathrm{i}kr\cos(\theta-\alpha)]. \tag{5}$$

Employing the Jacobi–Anger expansion (Abramowitz & Stegun 1972), eq. (5) can be re-expressed as

$$u^F(r,\theta) = 2\sum_{n=0}^{\infty}\varepsilon_n(-1)^n J_{2n}(kr)\cos(2n)\alpha\cos(2n)\theta - 4\mathrm{i}\sum_{n=0}^{\infty}(-1)^n J_{2n+1}(kr)\sin(2n+1)\alpha\sin(2n+1)\theta, \tag{6}$$

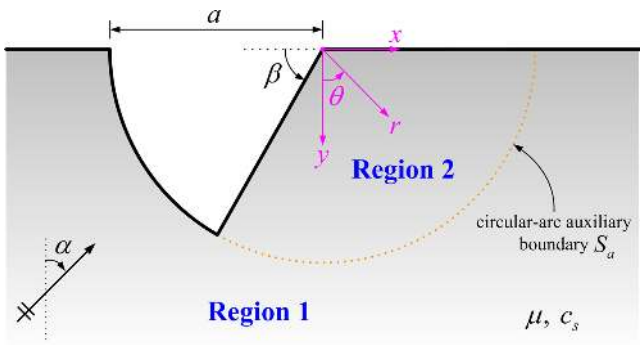

Figure 1. Geometric layout of the problem.

where ε_n is the Neumann factor (equal to 1 if $n = 0$ and to 2 if $n \geq 1$) and $J_n(\cdot)$ denotes the nth order Bessel function of the first kind. Note that this expression inherently satisfies the stress-free condition on the horizontal ground surface (eq. 2).

The *total* scattered field u^S in open region 1 may be separated into two parts, u^{S0} and u^{S2}, that is, $u^S = u^{S0} + u^{S2}$. The first part u^{S0} represents the scattered fields excluding the effect of region 2, and it also corresponds to the scattered fields derived by Trifunac (1973) for a semi-circular canyon, that is,

$$u^{S0}(r,\theta) = -2\sum_{n=0}^{\infty} \varepsilon_n (-1)^n \frac{J'_{2n}(ka)}{H^{(2)\prime}_{2n}(ka)} H^{(2)}_{2n}(kr)\cos(2n)\alpha\cos(2n)\theta + 4\mathrm{i}\sum_{n=0}^{\infty}(-1)^n \frac{J'_{2n+1}(ka)}{H^{(2)\prime}_{2n+1}(ka)} H^{(2)}_{2n+1}(kr)\sin(2n+1)\alpha \times \sin(2n+1)\theta, \quad (7)$$

where $H^{(2)}_n(\cdot)$ is the nth order Hankel function of the second kind, and primes stand for differentiation with respect to the argument of respective functions.

The second part u^{S2} is the contribution due to the presence of region 2. Through satisfying the governing Helmholtz equation (eq. 1) and the zero-stress conditions on the horizontal ground surface (eq. 2), and then taking account of the outgoing scattered waves, the scattered wavefield u^{S2} can be written as

$$u^{S2}(r,\theta) = \sum_{n=0}^{\infty} A_n \frac{H^{(2)}_{2n}(kr)}{H^{(2)\prime}_{2n}(ka)}\cos(2n)\theta + \sum_{n=0}^{\infty} B_n \frac{H^{(2)}_{2n+1}(kr)}{H^{(2)\prime}_{2n+1}(ka)}\sin(2n+1)\theta, \quad (8)$$

where the complex expansion coefficients A_n and B_n are unknown.

The displacement of the resultant wavefield u_1 in the open region 1, which is the combination of free and scattered wavefields, can be expressed as

$$u_1(r,\theta) = u^F(r,\theta) + u^S(r,\theta) \quad (9)$$

In the enclosed region 2, the displacement of wavefield u_2, satisfying the Helmholtz equation (eq. 1) and the traction-free conditions (eq. 4), is given by

$$u_2(r,\theta) = \sum_{n=0}^{\infty} C_n \frac{J_{n\nu}(kr)}{J'_{n\nu}(ka)}\cos n\nu\left(\theta - \frac{\pi}{2}\right), \quad (10)$$

in which $\nu = \pi/(\pi - \beta)$ and the complex expansion coefficients C_n are to be determined. More details for the derivation of eq. (10) are set out in Appendix A.

The radial stress must be continuous over the entire auxiliary boundary S_a, implying

$$\frac{\partial u_1}{\partial r} = \frac{\partial u_2}{\partial r} = \begin{cases} P(\theta), & -\frac{\pi}{2} + \beta < \theta < \frac{\pi}{2}, \\ 0, & -\frac{\pi}{2} < \theta < -\frac{\pi}{2} + \beta, \end{cases} \quad r = a, \quad (11)$$

Notice that the introduction of the stress function $P(\theta)$ may allow one to include the stress singularity (near the canyon bottom) in the later formulation.

Multiplying both sides of eq. (11) by the proper cosine/sine functions, and integrating over the corresponding ranges gives

$$\int_{-\frac{\pi}{2}}^{\frac{\pi}{2}} \frac{\partial u_1}{\partial r}\cos(2q)\theta\,\mathrm{d}\theta = \int_{-\frac{\pi}{2}+\beta}^{\frac{\pi}{2}} P(\theta)\cos(2q)\theta\,\mathrm{d}\theta, \quad q = 0, 1, \ldots, \quad (12)$$

$$\int_{-\frac{\pi}{2}}^{\frac{\pi}{2}} \frac{\partial u_1}{\partial r}\sin(2q+1)\theta\,\mathrm{d}\theta = \int_{-\frac{\pi}{2}+\beta}^{\frac{\pi}{2}} P(\theta)\sin(2q+1)\theta\,\mathrm{d}\theta, \quad q = 0, 1, \ldots, \quad (13)$$

$$\int_{-\frac{\pi}{2}+\beta}^{\frac{\pi}{2}} \frac{\partial u_2}{\partial r}\cos q\nu\left(\theta - \frac{\pi}{2}\right)\mathrm{d}\theta = \int_{-\frac{\pi}{2}+\beta}^{\frac{\pi}{2}} P(\theta)\cos q\nu\left(\theta - \frac{\pi}{2}\right)\mathrm{d}\theta, \quad q = 0, 1, \ldots. \quad (14)$$

After some algebra, it can be shown that

$$A_n = \frac{\varepsilon_n}{\pi}\hat{P}^{C1}_n, \quad (15)$$

$$B_n = \frac{2}{\pi}\hat{P}^{S}_n, \quad (16)$$

$$C_n = \frac{\varepsilon_n}{\pi - \beta}\hat{P}^{C2}_n, \quad (17)$$

where the transformed functions $\hat{P}^{C1}_n$, $\hat{P}^{C2}_n$ and $\hat{P}^{S}_n$ are as follows:

$$\hat{P}^{C1}_n = \int_{-\frac{\pi}{2}+\beta}^{\frac{\pi}{2}} P(\theta)\cos(2n)\theta\,\mathrm{d}\theta, \quad (18)$$

$$\hat{P}^{C2}_n = \int_{-\frac{\pi}{2}+\beta}^{\frac{\pi}{2}} P(\theta)\cos n\nu\left(\theta - \frac{\pi}{2}\right)\mathrm{d}\theta, \quad (19)$$

$$\hat{P}^{S}_n = \int_{-\frac{\pi}{2}+\beta}^{\frac{\pi}{2}} P(\theta)\sin(2n+1)\theta\,\mathrm{d}\theta. \quad (20)$$

To make progress and achieve numerical efficiency, the stress function $P(\theta)$ may be expanded in a series of basis functions, containing pivotal information on the behaviour of stress fields at the auxiliary boundary S_a. Hence, $P(\theta)$ may be approximated as follows:

$$P(\theta) = \sum_{m=0}^{\infty} p_m S_m(\theta), \quad (21)$$

where p_m are the singular expansion coefficients to be determined, and $S_m(\theta)$ are the singular basis functions.

At a salient corner with an interior angle of 90°, $P(\theta)$ has a singular behaviour of the form $r^{-1/3}$ as the radial distance r from the endpoint tends to zero (see Appendix B for details). Pondering over the singular nature of the corner point at $\theta = -\pi/2 + \beta$, and taking the traction-free condition into account, a set of appropriate basis functions satisfying the *correct* inverse cubic-root singularity is given by

$$S_m(\theta) = \psi_m \frac{C^{1/6}_{2m}[2\theta - \pi/2(\pi - \beta)]}{\{(\theta + \pi/2 - \beta)[3\pi - 2(\beta + \theta)](\pi - \beta)/2\}^{1/3}}, \quad (22)$$

where $\psi_m = (2m)!\Gamma(1/6)[\pi\Gamma(2m + 1/3)]^{-1}$, $\Gamma(\cdot)$ denotes the gamma functions, and $C^{1/6}_{2m}[\cdot]$ are the Gegenbauer polynomials typically having the following property (see, e.g. Gradshteyn & Ryzhik 2007, pp. 798, eq. 7.324):

$$\int_0^1 \frac{C^{1/6}_{2m}(\sigma)\cos(h\sigma)}{(1-\sigma^2)^{1/3}}d\sigma = \frac{\pi(-1)^m\Gamma(2m + 1/3)}{(2m)!\Gamma(1/6)(2h)^{1/6}}J_{2m+1/6}(h). \quad (23)$$

Additional remarks pertaining to the selection of singular basis functions are given in Appendix C.

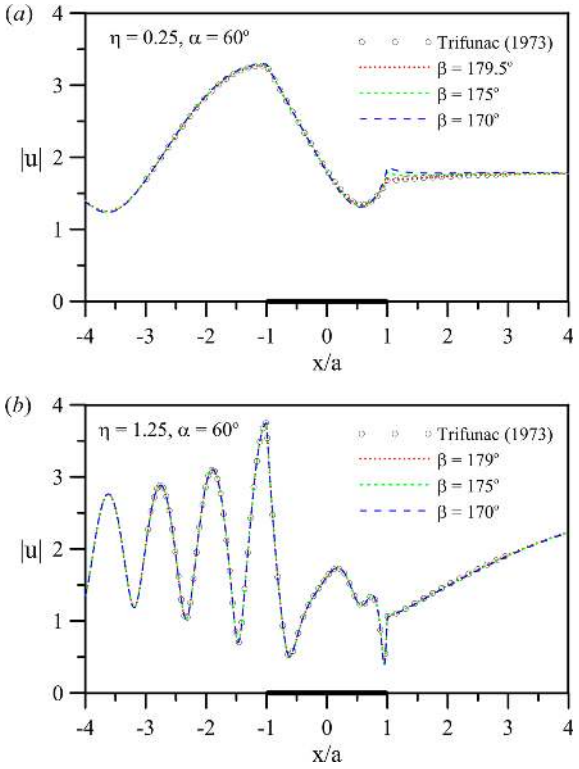

Figure 2. Surface motions versus x/a at $\alpha = 60^\circ$ for comparison with the results of Trifunac (1973). (a) $\eta = 0.25$; (b) $\eta = 1.25$.

After substituting eqs (21) and (22) into (18)–(20), one may find that the execution of Fourier cosine/sine transforms to the singular basis functions $S_m(\theta)$ is required. Using the change of variables and employing eq. (23), three integral transforms of $S_m(\theta)$ may be written, respectively, as follows:

$$\int_{-\frac{\pi}{2}+\beta}^{\frac{\pi}{2}} S_m(\theta)\cos(2n)\theta \mathrm{d}\theta = (-1)^{m+n}\frac{J_{2m+1/6}\,[2n(\pi-\beta)]}{[4n(\pi-\beta)]^{1/6}}, \tag{24}$$

$$\int_{-\frac{\pi}{2}+\beta}^{\frac{\pi}{2}} S_m(\theta)\cos n\nu\left(\theta-\frac{\pi}{2}\right)\mathrm{d}\theta = (-1)^{m}\frac{J_{2m+1/6}(n\pi)}{(2n\pi)^{1/6}}, \tag{25}$$

$$\int_{-\frac{\pi}{2}+\beta}^{\frac{\pi}{2}} S_m(\theta)\sin(2n+1)\theta \mathrm{d}\theta = (-1)^{m+n}\frac{J_{2m+1/6}\,[(2n+1)(\pi-\beta)]}{[(4n+2)(\pi-\beta)]^{1/6}}. \tag{26}$$

In the light of eqs (24)–(26), the transformed functions shown in eqs (18)–(20) may be expressed as follows:

$$\hat{P}_n^{C1} = \sum_{m=0}^{\infty} p_m(-1)^{m+n}\frac{J_{2m+1/6}\,[2n(\pi-\beta)]}{[4n(\pi-\beta)]^{1/6}}, \quad n \geq 1, \tag{27}$$

$$\hat{P}_n^{C2} = \sum_{m=0}^{\infty} p_m(-1)^{m}\frac{J_{2m+1/6}(n\pi)}{(2n\pi)^{1/6}}, \quad n \geq 1, \tag{28}$$

$$\hat{P}_n^{S} = \sum_{m=0}^{\infty} p_m(-1)^{m+n}\frac{J_{2m+1/6}\,[(2n+1)(\pi-\beta)]}{[(4n+2)(\pi-\beta)]^{1/6}}. \tag{29}$$

Table 1. Calculated results of the first components of wavefield expansion coefficients for $\beta = 45^\circ$ at $\alpha = 30^\circ$ and $\eta = 2$.

	Accurate RMT		
M	A_0	B_0	C_0
12	1.71507486 + 0.25135313i	2.11465312 − 1.24052281i	2.28676648 + 0.33513751i
20	1.71508502 + 0.25134337i	2.11464785 − 1.24054703i	2.28678003 + 0.33512449i
30	1.71508493 + 0.25134327i	2.11464762 − 1.24054697i	2.28677990 + 0.33512436i
42	1.71508493 + 0.25134325i	2.11464759 − 1.24054699i	2.28677991 + 0.33512434i
44	1.71508493 + 0.25134325i	2.11464759 − 1.24054699i	2.28677991 + 0.33512434i
	RMT		
50	1.71410826 + 0.25166114i	2.11460540 − 1.23928226i	2.28547768 + 0.33554819i
100	1.71472627 + 0.25143148i	2.11458908 − 1.24009935i	2.28630169 + 0.33524197i
500	1.71504652 + 0.25134894i	2.11463564 − 1.24050127i	2.28672869 + 0.33513192i
1000	1.71506992 + 0.25134519i	2.11464250 − 1.24052929i	2.28675990 + 0.33512692i

Table 2. Calculated results of the first components of wavefield expansion coefficients for $\beta = 45^\circ$ at $\alpha = 30^\circ$ and $\eta = 12$.

	Accurate RMT		
M	A_0	B_0	C_0
49	7.17640661 + 1.61364908i	6.83176172 − 3.95258994i	9.56854215 + 2.15153210i
60	7.17641493 + 1.61364728i	6.83176459 − 3.95259864i	9.56855324 + 2.15152970i
75	7.17641454 + 1.61364657i	6.83176375 − 3.95259869i	9.56855272 + 2.15152876i
95	7.17641426 + 1.61364619i	6.83176326 − 3.95259866i	9.56855235 + 2.15152825i
98	7.17641426 + 1.61364619i	6.83176326 − 3.95259866i	9.56855235 + 2.15152825i
	RMT		
50	7.18656337 + 1.62708650i	6.84934638 − 3.95397975i	9.58208449 + 2.16944867i
100	7.17872288 + 1.61751378i	6.83646096 − 3.95243003i	9.57163051 + 2.15668504i
500	7.17654539 + 1.61393512i	6.83209015 − 3.95254680i	9.56872718 + 2.15191350i
1000	7.17645845 + 1.61375043i	6.83187938 − 3.95257697i	9.56861126 + 2.15166723i

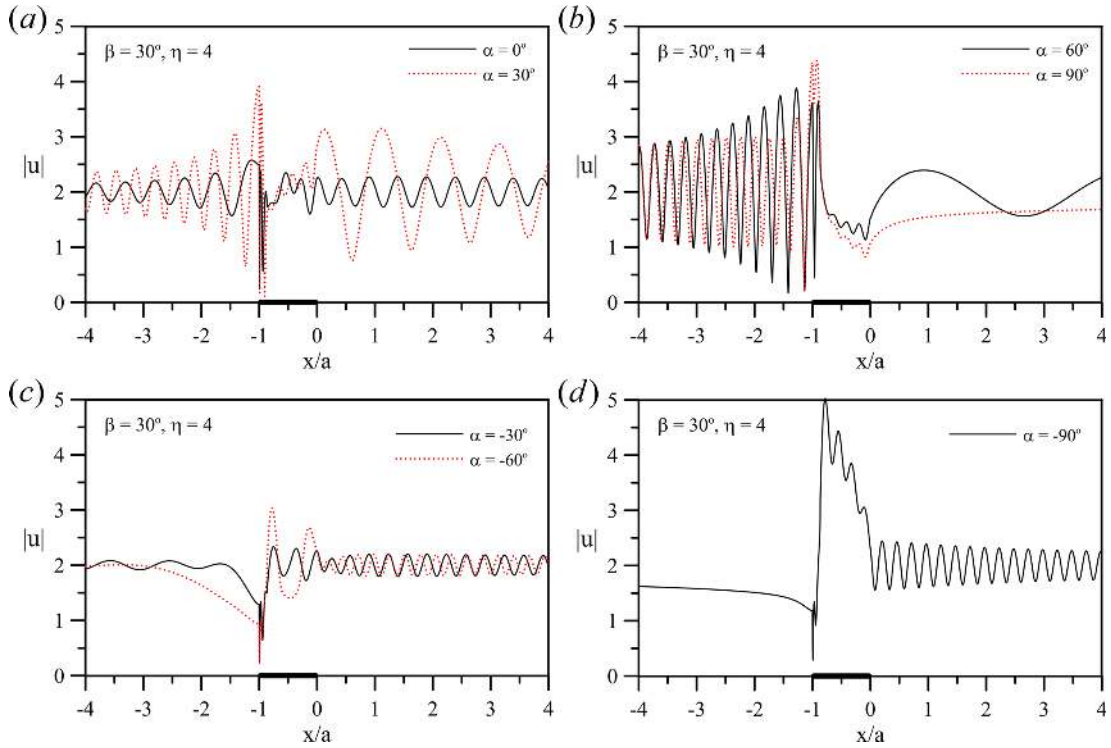

Figure 3. Surface motions versus x/a for different α with $\beta = 30^\circ$ at $\eta = 4$. (a) $\alpha = 0^\circ$ and 30°; (b) $\alpha = 60^\circ$ and 90°; (c) $\alpha = -30^\circ$ and -60°; (d) $\alpha = -90^\circ$.

Note that if $n = 0$, eqs (27) and (28) have the following forms:

$$\hat{P}_0^{C1} = \frac{6}{2^{1/3}\Gamma(1/6)} p_0, \tag{30}$$

$$\hat{P}_0^{C2} = \frac{6}{2^{1/3}\Gamma(1/6)} p_0. \tag{31}$$

Substitution of eqs (27)–(31) into (15)–(17) leads to the connection between the expansion coefficients of displacement fields (A_n, B_n and C_n) and those of corner singularity (p_m), that is,

$$A_0 = \frac{6}{\pi\ 2^{1/3}\ \Gamma(1/6)} p_0, \tag{32}$$

$$A_n = \frac{2}{\pi} \sum_{m=0}^{\infty} p_m (-1)^{m+n} \frac{J_{2m+1/6}\,[2n(\pi-\beta)]}{[4n(\pi-\beta)]^{1/6}}, \quad n \geq 1, \tag{33}$$

$$B_n = \frac{2}{\pi} \sum_{m=0}^{\infty} p_m (-1)^{m+n} \frac{J_{2m+1/6}\,[(2n+1)(\pi-\beta)]}{[(4n+2)(\pi-\beta)]^{1/6}} \tag{34}$$

$$C_0 = \frac{6}{(\pi-\beta)\ 2^{1/3}\ \Gamma(1/6)} p_0, \tag{35}$$

$$C_n = \frac{2}{\pi-\beta} \sum_{m=0}^{\infty} p_m (-1)^{m} \frac{J_{2m+1/6}(n\pi)}{(2n\pi)^{1/6}}, \quad n \geq 1. \tag{36}$$

For the sake of determining the singular expansion coefficients p_m, the enforcement of displacement continuity condition across the auxiliary boundary S_a is necessary, that is,

$$u_1(r,\theta) = u_2(r,\theta), \quad \text{for} \quad -\frac{\pi}{2} + \beta < \theta < \frac{\pi}{2} \quad \text{and} \quad r = a. \tag{37}$$

Multiplying eq. (37) by a sequence of testing functions and integrating over the range $[-\pi/2 + \beta, \pi/2]$ gives

$$\int_{-\frac{\pi}{2}+\beta}^{\frac{\pi}{2}} u_1\, S_q(\theta)\, \mathrm{d}\theta = \int_{-\frac{\pi}{2}+\beta}^{\frac{\pi}{2}} u_2\, S_q(\theta)\, \mathrm{d}\theta, \quad q = 0, 1, \ldots. \tag{38}$$

Substituting eqs (9), (10) and (32)–(36) into (38), utilizing the Wronskian relations (Abramowitz & Stegun 1972), applying eqs (24)–(26) and rearranging yields a system of linear algebraic equations for singular coefficients p_m, that is,

$$\sum_{m=0}^{\infty} p_m U_{q,m} = V_q, \quad q = 0, 1, \ldots, \tag{39}$$

where all the involved functions are given in Appendix D (see eqs D1 and D2). After truncating the infinite series properly, the singular expansion coefficients p_m can be evaluated by the standard matrix techniques.

For numerical computation, truncating the infinite summation to a finite number of terms is indispensable. In eq. (39), the summation indices m and the weighting indices q are truncated after $M - 1$ terms. Therefore, eq. (39) constitutes a system of M equations with M unknowns. The number of truncation terms in consideration depends only on the accuracy requirement. Once the singular coefficients p_m are found, the wavefield expansion coefficients (i.e. A_n, B_n and C_n) can be evaluated straightforwardly via eqs (32)–(36).

3 NUMERICAL RESULTS AND DISCUSSIONS

To get the proper truncation value M in eq. (39), a number of convergence tests are carried out first. It is worth emphasizing that each

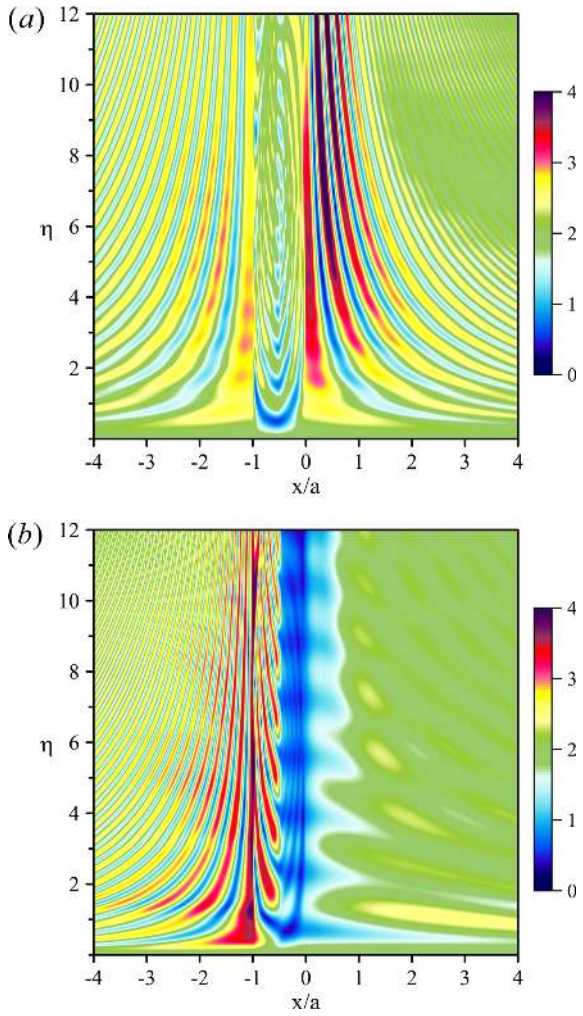

Figure 4. Spectral variations in surface motions around the canyon with $\beta = 60^\circ$ at (a) $\alpha = 0^\circ$ and (b) $\alpha = 45^\circ$.

inner sum with index n is truncated to N or $N-1$ terms (see eqs D3–D7 and D13–D15 in Appendix D), and it should be calculated accurately by numerical testing for its convergence, thereby leaving only one parameter (i.e. summation indices M) to remove the problem of relative convergence. Numerical experiments show that more terms are required as the wave frequency increases.

In the following, the dimensionless frequency η is defined as

$$\eta = \frac{ka}{\pi} = \frac{2a}{\lambda}. \tag{40}$$

3.1 Validation for the limiting case

When the size of region 2 becomes very small (i.e. $\beta \to 180^\circ$), the sectorial canyon approximates to the semi-circular one. Since Trifunac (1973) derived an exact analytical solution to antiplane scattering induced by a semi-circular canyon, several cases shown in figs 6 and 8 of Trifunac (1973) are taken as validation examples. Computed results pertinent to the case of $\eta = 0.25$ at oblique incidence ($\alpha = 60^\circ$) are given in Fig. 2(a), while those relative to the case of $\eta = 1.25$ in Fig. 2(b). Specific locations on the canyon surface ranging between $x/a = -1$ and 1 are displayed by a bold black line. Figs 2(a) and (b) exhibit good consistency between the present results and those of Trifunac (1973). Obviously, results ensure that there is no mistake in the formulism presented. In addition, one can find that at a relatively high frequency (see Fig. 2b), the results of this study are very close to those of Trifunac (1973) when the selected value of β is larger than 170°. However, at a relatively low frequency (see Fig. 2a), in order to arrive at a good approximation to the result of Trifunac (1973), β has to be larger than 179°. The reason is that the canyon can easily hamper the incident waves with relatively short wavelengths, and, therefore, only a small amount of scattered waves can penetrate into region 2.

3.2 Accuracy and performance of the accurate RMT

Tables 1 and 2 demonstrate three sets of computed values to the first components of wavefield expansion coefficients in regions 1 and 2 at oblique incidence ($\alpha = 30^\circ$). The central angle of the canyon is set to be $\beta = 45^\circ$. Table 1 corresponds to a low-frequency case ($\eta = 2$), while Table 2 to a high-frequency case ($\eta = 12$). To manifest the accuracy and efficiency of the accurate RMT, calculated results of the series solution derived by the RMT (see Appendix E) are also included in Tables 1 and 2.

As shown in Table 1, the accurate RMT guarantees 4-decimal place accuracy at $M = 12$ (a 12×12 matrix required), and 8-decimal place accuracy is attainable at $M = 42$ (a 42×42 matrix needed). When the wave frequency becomes higher (see Table 2), 4-decimal place accuracy can be achieved at $M = 49$, and 8-decimal place accuracy at $M = 95$. By contrast, results obtained by the RMT converge extremely slowly. The RMT gets only 4-decimal place accuracy at best for the low-frequency case, albeit a huge value of $M = 1000$ (a 1000×1000 matrix solved) adopted. As seen in Table 2, the RMT with a vast truncation value merely maintains 2- or 3-decimal place accuracy at a very high frequency. Undoubtedly, Tables 1 and 2 show that the employment of the accurate RMT is much more efficient than that of the RMT. The reason to get such good results is the inclusion of near-corner stress singularity in the solution procedure.

3.3 Surface and subsurface motions in the frequency domain

Fig. 3 displays the surface displacement amplitudes versus the dimensionless horizontal distance for seven incident angles at a relatively high frequency ($\eta = 4$). From Fig. 3, one can find that the relatively high levels of ground shaking are likely to occur frequently near the upper left corner (ULC) of the canyon. The maximum value of displacement amplitudes tends to increase as the angle of incidence bends towards the horizontal ground surface. Surface motions on the illuminated side become more oscillatory than those on the shielded side. For horizontal incidence ($\alpha = -90^\circ$) in Fig. 3(d), the peak amplitude can be up to about 2.5 times that of the free-field response.

For the sake of revealing the influence of dimensionless frequencies on surface motions, Fig. 4 gives the spectral variations in displacement amplitudes for vertical and oblique incidence (i.e. $\alpha = 0^\circ$ and 45°) with $\beta = 60^\circ$. As seen in Fig. 4(a), the upper right corner (URC) of the canyon ($0 < x/a < 0.5$) behaves as a concentrator collecting the wave energy, especially for the high-frequency cases ($6 < \eta < 12$). In Fig. 4(b), similar focusing phenomenon can also be observed at locations close to the ULC of the canyon. The amplification factor can reach the values of 2.3 and 2.0 for vertical and oblique incidence, respectively.

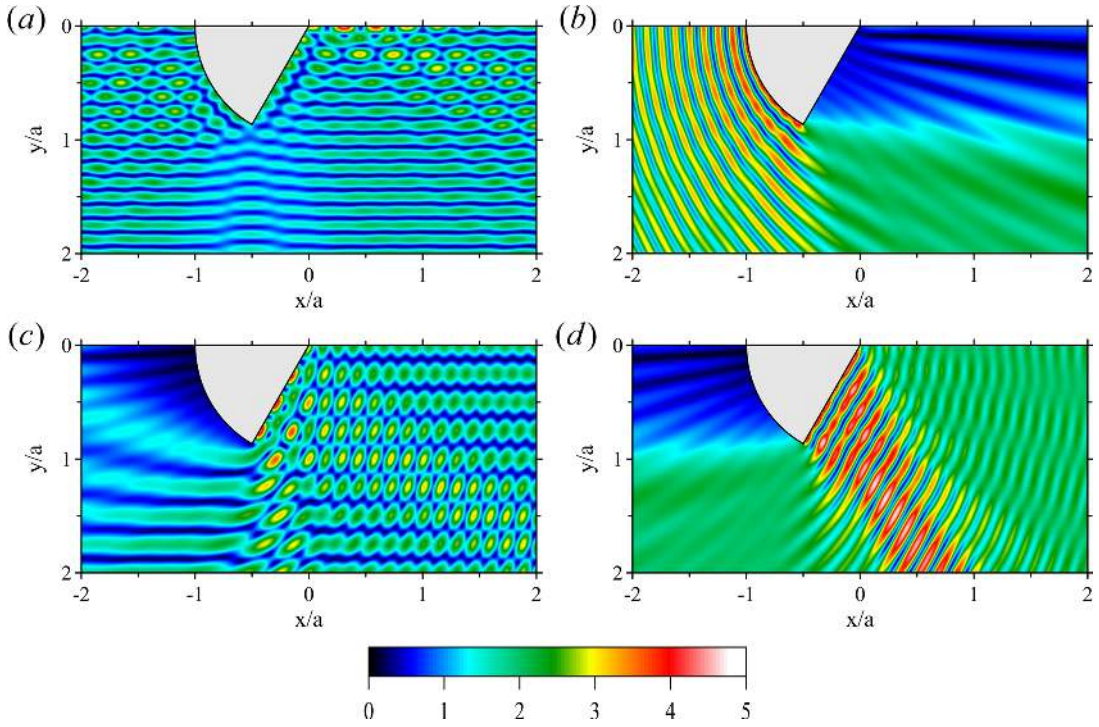

Figure 5. Subsurface motions around the canyon with $\beta = 60^\circ$ for $\eta = 8$. (a) $\alpha = 0^\circ$; (b) $\alpha = 90^\circ$; (c) $\alpha = -60^\circ$; (d) $\alpha = -90^\circ$.

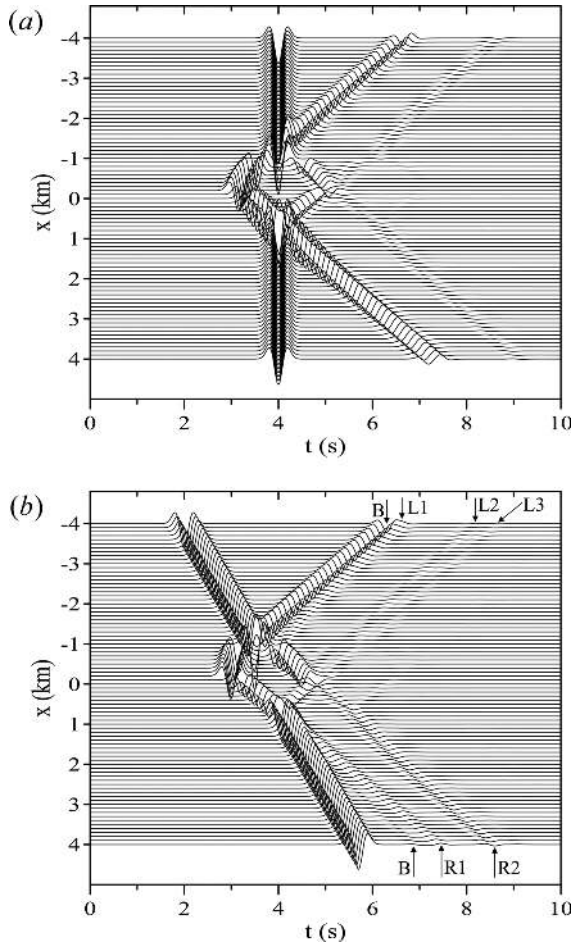

Figure 6. Synthetic seismograms for $f_c = 2\,\text{Hz}$ at $\beta = 60^\circ$. (a) $\alpha = 0^\circ$; (b) $\alpha = 30^\circ$.

Figs 5(a)–(d) exhibit the subsurface motions around the canyon at $\alpha = 0^\circ, 90^\circ, -60^\circ$ and -90°, respectively, when $\eta = 8$. The local maximum displacement amplitudes occur on the right-hand side of the flat ground surface for vertical incidence ($\alpha = 0^\circ$) in Fig. 5(a), and on the even surface of the canyon for oblique incidence in Fig. 5(c). For the case of horizontally incident waves (see Figs 5b and d), seismic motions in the illuminated region can be amplified at least two times more than those in the nearby region. This may be attributed to the constructive interference between the incident, reflected, and scattered waves.

Overall, surface and subsurface motions in the vicinity of the canyon are dependent not only on the central angle of the canyon but also on the frequency and angle of incidence of arriving waves.

3.4 Surface and subsurface motions in the time domain

Using the fast Fourier transform algorithm, one may pursue the time-domain responses from the preliminary results obtained in the frequency domain. The incident signal is a symmetric Ricker wavelet (Ricker 1945), which is defined to be

$$u(t) = (2\pi^2 f_c^2 t^2 - 1)\exp(-\pi^2 f_c^2 t^2), \tag{41}$$

where f_c is the characteristic frequency and is set to be 2 Hz here. Computations are made at a number of discrete frequencies ranging from 0 to 8 Hz with an interval of 0.0625 Hz. The time window is chosen as 16 s. The canyon radius a and shear-wave velocity c_s are set to be 1 km and 1 kms^{-1}, respectively. The central angle of the canyon is $\beta = 60^\circ$.

Fig. 6 displays two synthetic seismograms at vertical and oblique incidence ($\alpha = 0^\circ$ and 30°). At the top of Fig. 6(b), four signals received after the direct-wave signals are labelled, in turn, by arrows B, $L1$, $L2$ and $L3$, while at the bottom of Fig. 6(b), three signals are designated by arrows B, $R1$ and $R2$. From Figs 6(a) and (b), the amplifications of surface motions can be up to about 1.62 and 1.82

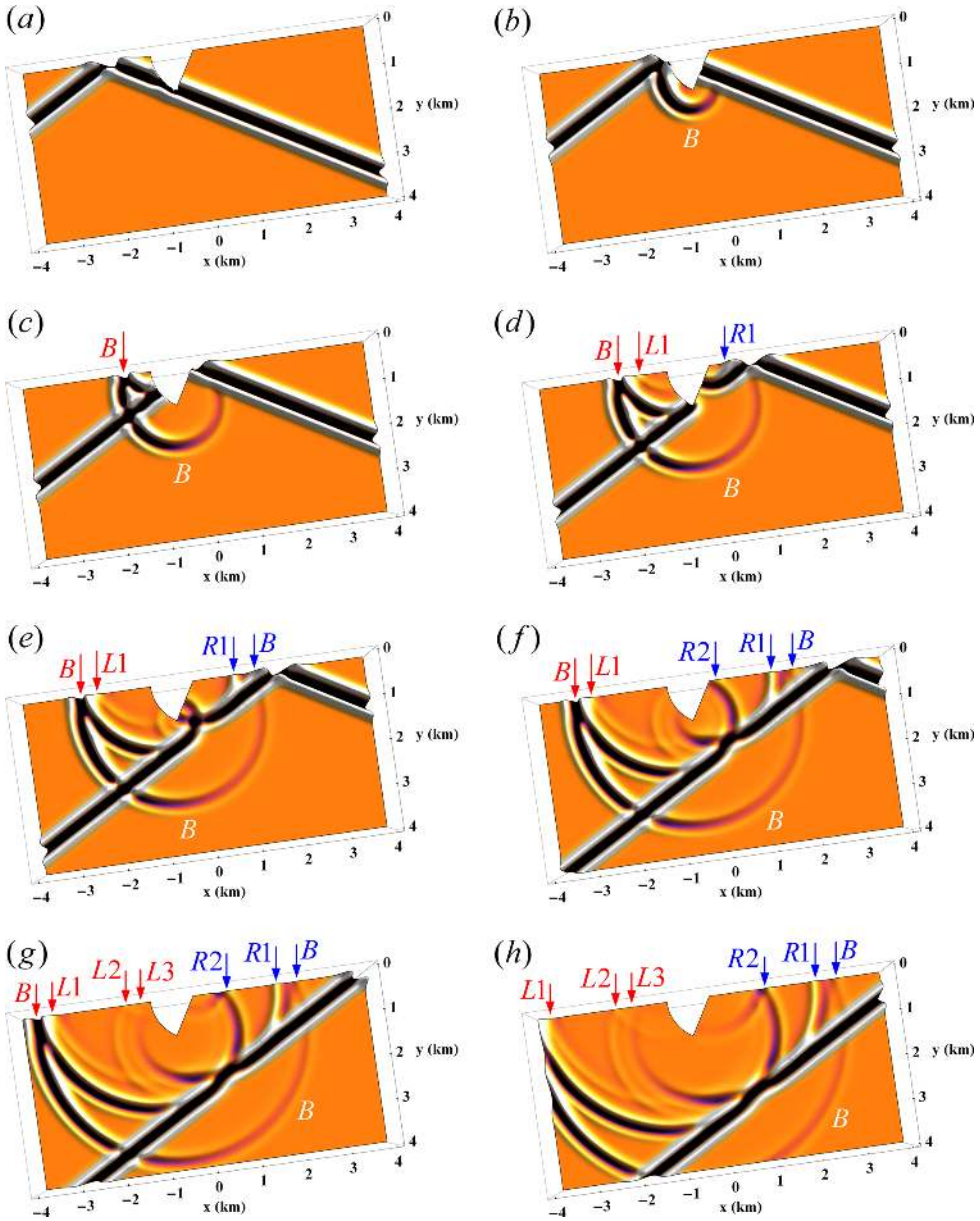

Figure 7. Snapshots for subsurface motions around the canyon with $\beta = 60°$ at $\alpha = 30°$. (a) $t = 3.0$ s; (b) $t = 3.5$ s; (c) $t = 4.0$ s; (d) $t = 4.5$ s; (e) $t = 5.0$ s; (f) $t = 5.5$ s; (g) $t = 6.0$ s; (h) $t = 6.5$ s.

times those of the free-field response under vertical and oblique incidence, respectively.

In order to show the discrimination between different signal sources, eight snapshots of transient subsurface motions at $\alpha = 30°$ are shown in Fig. 7. Furthermore, all arrows marked in Fig. 6(b) are appropriately tagged in Fig. 7. In Fig. 7(a), the incoming pulses impinge on the canyon bottom. In Fig. 7(b), a scattered wavetrain B (i.e. arrow B in Fig. 6b) radiates from the canyon bottom. In Fig. 7(c), the incident pulses reach the URC of the canyon. The scattered waves arising from the ULC of the canyon and the scattered waves B combine together on the left-hand side of the horizontal ground surface. Fig. 7(d) shows two new scattered waves (see arrows $L1$ and $R1$) radiated from the two upper corners of the canyon. In Figs 7(g) and (h), the scattered waves $L2$, $L3$ and $R2$ generate. The amplitudes of scattered waves $L2$ and $L3$ are smaller than those of $R2$.

In general, the bottom and two upper corners of the canyon behave as new wave sources. A key feature of the diffraction is that a part of the reflected wave front from the horizontal ground surface is cut off by the canyon and then continuously regenerates itself.

4 CONCLUSIONS

A rigorous series solution was derived for the *SH*-wave scattering by a circular sectorial canyon. A robust, accurate RMT proposed herein has successfully combined the RMT with the forethought of corner singularity. Selected basis functions explicitly include and can correctly model the known singularity in stress fields around the canyon bottom. A set of integral equations for stress fields at the auxiliary interface has been derived and then solved by the Galerkin method. Both the steady-state and transient variations in surface and

subsurface motions have been evaluated and analysed . Comparing with the computational results using the RMT, the accurate RMT indeed performs well without any excessive computational effort. Such a fast, convergent technique not only provides a reliable benchmark for assessing the results of other numerical approaches, but also has a promising potential to attack similar problems with troublesome geometric singularities.

ACKNOWLEDGEMENTS

The authors are deeply indebted to the Editor, Prof. Wolfgang Friederich and a reviewer for their encouragements and insightful and valuable suggestions and comments for improving this paper. Besides, the first and third authors sincerely appreciate the financial support granted by the National Science Council, Taiwan, R.O.C. (Project Nos. NSC 101–2811-M-001–167 and NSC 101–2116-M-001–015, respectively).

REFERENCES

Abramowitz, M. & Stegun, I.A., 1972. *Handbook of Mathematical Functions, with Formulas, Graphs, and Mathematical Tables,* Dover, New Yorks.

Arfken, G.B., Weber, H.J. & Harris, F.E., 2013. *Mathematical Methods for Physicists: A Comprehensive Guide,* 7th edn, Academic Press, USA.

Aki, K. & Larner, K.L., 1970. Surface motion of a layered medium having an irregular interface due to incident plane SH waves, *J. geophys. Res.,* **75,** 933–954.

Boore, D.M., 1973. The effect of simple topography on seismic waves: Implications for the accelerations recorded at Pacoima Dam, San Fernando Valley, California, *Bull. seism. Soc. Am.,* **63,** 1603–1609.

Bouchon, M., 1973. Effect of topography on surface motion, *Bull. seism. Soc. Am.,* **63,** 615–632.

Celebi, M., 1987. Topographical and geological amplifications determined from strong motion and aftershock records of the 3 March 1985 Chile earthquake, *Bull. seism. Soc. Am.,* **77,** 1147–1167.

Chang, K.H., 2009. Scattering and diffraction of plane SH waves by surface and subsurface truncated circular discontinuities, *PhD thesis,* National Taiwan Ocean University, Taiwan, pp. 200.

Davis, L.L. & West, L.R., 1973. Observed effects of topography on ground motion, *Bull. seism. Soc. Am.,* **63,** 283–298.

England, R., Sabina, F.J. & Herrera, I., 1980. Scattering of SH waves by surface cavities of arbitrary shape using boundary methods, *Phys. Earth Planet. Inter.,* **21,** 148–157.

Freund, L.B., 1998. *Dynamic Fracture Mechanics,* Cambridge University Press, Cambridge, UK.

Geli, L., Bard, P.Y. & Jullien, B., 1988. The effect of topography on earthquake ground motion: a review and new results, *Bull. seism. Soc. Am.,* **78,** 42–63.

Geller, R.J. & Takeuchi, N., 1998. Optimally accurate second-order time-domain finite difference scheme for the elastic equation of motion: one-dimensional case, *Geophys. J. Int.,* **135,** 48–62.

Gottlieb, D. & Shu, C.W., 1997. On the Gibbs phenomenon and its resolution, *SIAM Rev.,* **39,** 644–668.

Gradshteyn, I.S. & Ryzhik, I.M., 2007. *Table of Integrals, Series and Products,* 7th edn, Elsevier Inc., US, pp. 1170.

Hartzell, S.H., Carver, D.L. & King, K.W., 1994. Initial investigation of site and topographic effects at Robinwood Ridge, California, *Bull. seism. Soc. Am.,* **84,** 1336–1349.

Hough, S.E. *et al.*, 2010. Localized damage caused by topographic amplification during the 2010 M 7.0 Haiti earthquake, *Nat. Geosc.,* **3,** 778–782.

Ichimura, T., Hori, M. & Kuwamoto, H., 2007. Earthquake motion simulation with multiscale finite-element analysis on hybrid grid, *Bull. seism. Soc. Am.,* **97,** 1133–1143.

Jeffrey, A. & Dai, H.H., 2008. *Handbook of Mathematical Formulas and Integrals,* 4th edn, Academic Press, USA.

Käser, M. & Dumbser, M., 2006. An Arbitrary high order discontinuous galerkin method for elastic waves on unstructured meshes—I. The two-dimensional isotropic case with external source terms, *Geophys. J. Int.,* **166,** 855–877.

Kawase, H. & Aki, K., 1990. Topography effect at the critical SV wave incidence: possible explanation of damage pattern by the Whittier-Narrows, California, earthquake of 1 October 1987, *Bull. seism. Soc. Am.,* **80,** 1–22.

Kham, M., Semblat, J.F., Bard, P.Y. & Dangla, P., 2006. Seismic site-city interaction: main governing phenomena through simplified numerical models, *Bull. seism. Soc. Am.,* **96,** 1934–1951.

Komatitsch, D. & Vilotte, J.P., 1998. The spectral element method: an efficient tool to simulate the seismic response of 2D and 3D geological structures, *Bull. seism. Soc. Am.,* **88,** 368–392.

Kristek, J., Moczo, P. & Galis, M., 2010. Stable discontinuous staggered grid in the finite-difference modelling of seismic motion, *Geophys. J. Int.,* **183,** 1401–1407.

Lee, S.J., Chen, H.W. & Huang, B.S., 2008. Simulations of strong ground motion and 3D amplification effect in the Taipei basin by using a composite grid finite-difference method, *Bull. seism. Soc. Am.,* **98,** 1229–1242.

Lee, S.J., Chan, Y.C., Komatitsch, D., Huang, B.S. & Tromp, J., 2009. Effects of realistic surface topography on seismic ground motion in the Yangminshan region of Taiwan based upon the spectral-element method and LiDAR DTM, *Bull. seism. Soc. Am.,* **99,** 681–693.

Lombard, B., Piraux, J., Gélis, C. & Virieux, J., 2008. Free and smooth boundaries in 2-D finite-difference schemes for transient elastic waves, *Geophys. J. Int.,* **172,** 252–261.

Ma, S., Archuleta, R.J. & Page, M.T., 2007. Effects of large-scale surface topography on ground motions, as demonstrated by a study of the San Gabriel Mountains, Los Angeles, California, *Bull. seism. Soc. Am.,* **97,** 2066–2079.

Pivato, M., 2010. *Linear Partial Differential Equations and Fourier Theory,* Cambridge University Press, Cambridge, UK.

Pelties, C., Käser, M., Hermann, V. & Castro, C.E., 2010. Regular versus irregular meshing for complicated models and their effect on synthetic seismograms, *Geophys. J. Int.,* **183,** 1031–1051.

Ricker, N., 1945. The computation of output disturbances from amplifiers for true wavelet inputs, *Geophysics,* **10,** 207–220.

Sánchez-Sesma, F.J. & Rosenblueth, E., 1979. Ground motion at canyons of arbitrary shape under incident SH waves, *Earthq. Eng. Struct. Dynam.,* **7,** 441–450.

Sánchez-Sesma, F.J., Palencia, V.J. & Luzón, F., 2002. Estimation of local site effects during earthquakes: an overview, *ISET J. Earthq. Technol.,* **39,** 167–193.

Satoh, T., Kawase, H., Sato, T. & Pitarka, A., 2001. Three-dimensional finite difference waveform modeling of strong motions observed in the Sendai basin, Japan, *Bull. seism. Soc. Am.,* **91,** 812–825.

Scott, A.A., Sitar, N., Lysmer, J. & Deng, N., 1997. Topographic effects on the seismic response of steep slopes, *Bull. seism. Soc. Am.,* **87,** 701–709.

Spudich, P., Hellweg, M. & Lee, W.H.K., 1996. Directional topographic site response at Tarzana observed in aftershocks of the 1994 Northridge, California earthquake: implications for mainshock motions, *Bull. seism. Soc. Am.,* **86,** S193–S208.

Tessmer, E., Kosloff, D. & Behle, A., 1992. Elastic wave-propagation simulation in the presence of surface-topography, *Geophys. J. Int.,* **108,** 621–632.

Trifunac, M.D., 1973. Scattering of plane SH waves by a semi-cylindrical canyon, *Earthq. Eng. Struct. Dynam.,* **1,** 267–281.

Tsaur, D.H. & Chang, K.H., 2008. An analytical approach for the scattering of SH waves by a symmetrical V-shaped canyon: shallow case, *Geophys. J. Int.,* **174,** 255–264.

Tsaur, D.H. & Chang, K.H., 2009. Scattering and focusing of SH waves by a convex circular-arc topography, *Geophys. J. Int.,* **177,** 222–234.

Tsaur, D.H., Chang, K.H. & Hsu, M.S., 2010. An analytical approach for the scattering of SH waves by a symmetrical V-shaped canyon: deep case, *Geophys. J. Int.,* **183,** 1501–1511.

Tsaur, D.H., 2011. Scattering and focusing of SH waves by a lower semielliptic convex topography, *Bull. seism. Soc. Am.,* **101,** 2212–2219.

Tsaur, D.H., Chang, K.H. & Hsu, M.S., 2011. A series solution for the diffraction of SH waves by a vertical edge crack, *J. Appl. Mech.,* **78,** 044502, doi:10.1115/1.4003745.

Tsaur, D.H. & Hsu, M.S., 2013. SH waves scattering from a partially filled semi-elliptic alluvial valley, *Geophys. J. Int.,* **194,** 499–511.

Wong, H.L. & Trifunac, M.D., 1974. Scattering of plane SH waves by a semi-elliptical canyon, *Earthq. Eng. Struct. Dynam.,* **3,** 157–169.

Wong, H.L. & Jennings, P.C., 1975. Effects of topography on strong ground motion, *Bull. seism. Soc. Am.,* **65,** 1239–1257.

Zargano, G.F., Lerer, A.M. & Lyapin, A.M., 1979. *Waveguides of Compound Cross-sections,* Rostov University Press, Rostov-na-Donu, former USSR (In Russian).

Zhou, H. & Chen, X., 2006. A new approach to simulate scattering of SH waves by an irregular topography, *Geophys. J. Int.,* **164,** 449–459.

APPENDIX A: DERIVATION OF EQ (10)

For the enclosed region 2, eq. (1) written in polar coordinates takes the following form

$$\frac{1}{r}\frac{\partial}{\partial r}\left(r\frac{\partial u_2}{\partial r}\right)+\frac{1}{r^2}\frac{\partial^2 u_2}{\partial \theta^2}+k^2u_2=0. \tag{A1}$$

Using the MSV (see e.g. Pivato 2010, section 16C; Arfken *et al.* 2013, section 9.4), we take a separated solution in the form

$$u_2(r,\theta)=R(r)\Phi(\theta), \tag{A2}$$

with the separation constant as $\tilde{\nu}^2$, we can decompose eq. (A1) into two linear homogeneous ordinary differential equations in r and θ, respectively:

$$R''(r)+r^{-1}R'(r)+\left(k^2-\frac{\tilde{\nu}^2}{r^2}\right)R(r)=0, \tag{A3}$$

$$\Phi''(\theta)+\tilde{\nu}^2\,\Phi(\theta)=0. \tag{A4}$$

The radial part (eq. A3) can be easily transformed into Bessel's differential equation. Taking into account the fact that the solution has to be finite at the origin $r=0$, and consequently getting rid of the terms involving Bessel functions of the second kind, the general solution of eq. (A3) can be expressed as

$$R(r)=c_1J_{\tilde{\nu}}(kr), \tag{A5}$$

in which c_1 is the arbitrary constant.

On the other hand, the angular part (eq. A4) has the following family of solutions:

$$\Phi(\theta)=c_2\cos\tilde{\nu}\theta+c_3\sin\tilde{\nu}\theta, \tag{A6}$$

where c_2 and c_3 are arbitrary constants. Applying the zero-stress condition at $\theta=\pi/2$, inserting eq. (4) into eq. (A6) leads to

$$c_2=c_3\frac{\cos(\tilde{\nu}\pi/2)}{\sin(\tilde{\nu}\pi/2)}. \tag{A7}$$

Employing eq. (A7), we may rewrite eq. (A6) as

$$\Phi(\theta)=\tilde{c}_3\cos\tilde{\nu}\left(\theta-\frac{\pi}{2}\right). \tag{A8}$$

In order to determine $\tilde{\nu}$, substituting eq. (A8) into the stress-free condition at $\theta=-\pi/2+\beta$, eq. (4), yields

$$\tilde{\nu}=\frac{n\,\pi}{\pi-\beta},\qquad n=0,1,\ldots. \tag{A9}$$

After setting $\tilde{\nu}=n\nu$, eqs (A5) and (A8) become the building blocks with which we construct the general solution for region 2 by linear superposition, that is, eq. (10).

APPENDIX B: SINGULAR STRESS FIELDS NEAR THE SALIENT CORNER

In order to reveal the existence of stress singularity in the vicinity of the canyon bottom, we turn to the derivation of stress fields in a wedge-shaped region (with an internal angle of $2\pi-2\hat{\beta}$). Referring to the geometric layout shown in fig. 1 of Tsaur & Chang (2008) (or that in fig. 1 of Tsaur *et al.* 2010) and following eq. (13) of Tsaur & Chang (2008) (or eq. 10 of Tsaur *et al.* 2010), the antiplane displacement fields within the region 2 (i.e. corner region) can be expressed as

$$\hat{u}_2(r_1,\theta_1)=\sum_{n=0}^{\infty}\hat{C}_nJ_{2n\,\hat{\nu}}(kr_1)\cos(2n)\hat{\nu}\theta_1 + \sum_{n=0}^{\infty}\hat{D}_nJ_{(2n+1)\hat{\nu}}(kr_1)\sin(2n+1)\hat{\nu}\theta_1, \tag{B1}$$

where $\hat{\nu}=\pi/(2\hat{\beta})$ and r_1 is the radial distance from the apex of the wedge to the observed point. Note that eq. (B1) intrinsically satisfies the Helmholtz equation and the zero-stress conditions on both sides of the corner region.

As to the stress fields, their components in the radial and circumferential directions can be written, respectively, as

$$\hat{\tau}^{(2)}_{r_1z}=\mu\frac{\partial\hat{u}_2}{\partial r_1}(r_1,\theta_1), \tag{B2}$$

$$\hat{\tau}^{(2)}_{\theta_1z}=\frac{\mu}{r_1}\frac{\partial\hat{u}_2}{\partial\theta_1}(r_1,\theta_1). \tag{B3}$$

Substituting eq. (B1) into (B2) gives

$$\hat{\tau}^{(2)}_{r_1z}(r_1,\theta_1)=\frac{k\mu}{2}\sum_{n=0}^{\infty}\hat{C}_nJ_{2n\,\hat{\nu}-1}(kr_1)\cos(2n)\hat{\nu}\,\theta_1 - \frac{k\mu}{2}\sum_{n=0}^{\infty}\hat{C}_nJ_{2n\,\hat{\nu}+1}(kr_1)\cos(2n)\hat{\nu}\,\theta_1 + \frac{k\mu}{2}\sum_{n=0}^{\infty}\hat{D}_nJ_{(2n+1)\hat{\nu}-1}(kr_1)\sin(2n+1)\hat{\nu}\,\theta_1 - \frac{k\mu}{2}\sum_{n=0}^{\infty}\hat{D}_nJ_{(2n+1)\hat{\nu}+1}(kr_1)\sin(2n+1)\hat{\nu}\,\theta_1. \tag{B4}$$

Accordingly, substituting eq. (B1) into (B3) yields

$$\hat{\tau}^{(2)}_{\theta_1z}(r_1,\theta_1)=-\frac{2\mu\hat{\nu}}{r_1}\sum_{n=0}^{\infty}n\,\hat{C}_nJ_{2n\,\hat{\nu}}(kr_1)\sin(2n)\hat{\nu}\,\theta_1 + \frac{\mu\hat{\nu}}{r_1}\sum_{n=0}^{\infty}(2n+1)\,\hat{D}_nJ_{(2n+1)\hat{\nu}}(kr_1)\cos(2n+1)\hat{\nu}\,\theta_1. \tag{B5}$$

From the power-series expansion for Bessel functions of the first kind (e.g. Jeffrey & Dai 2008, pp. 291, section 17.2.1.1, eq. 6), we have

$$J_\zeta(\varphi)=\left(\frac{\varphi}{2}\right)^{\zeta}\sum_{m=0}^{\infty}\frac{(-1)^m}{m!\;\Gamma(\zeta+m+1)}\left(\frac{\varphi}{2}\right)^{2m}. \tag{B6}$$

For $-1<\zeta<0$, the leading term tends to an unbounded value when the argument φ approaches zero, indicating the existence of a singularity of the type φ^{ζ}. From eq. (B6), the stress fields around the corner point can be expressed as a power series in r_1.

Applying eq. (B6) to (B4) and (B5), one can easily find that for radial stresses close to the tip of the wedge, the dominant singularity arises in the first term of the third infinite series on the right-hand side (RHS) of eq. (B4). Similarly, for angular stresses, a singularity exists due to the first term of the second infinite sum on the RHS of eq. (B5). These imply that the extremely near-field behaviour of stress components in the neighbourhood of the corner point should have the following forms:

$$\lim_{r_1 \to 0} \hat{\tau}^{(2)}_{r_1 z}(r_1, \theta_1) = \mathcal{O}(r_1^{\hat{\nu}-1}), \tag{B7}$$

$$\lim_{r_1 \to 0} \hat{\tau}^{(2)}_{\theta_1 z}(r_1, \theta_1) = \mathcal{O}(r_1^{\hat{\nu}-1}), \tag{B8}$$

where $\hat{\nu} - 1$ stands for the order of stress singularity.

Considering a special case of right-angled corners (i.e. $\hat{\beta} = 3\,\pi/4$ and $\hat{\nu} = 2/3$), the stress function $P(\theta)$ introduced in eq. (11) must behave like $r_1^{-1/3}$. On the other hand, a limiting case is present when both sides of the wedge coincide with each other (i.e. $\hat{\beta} = \pi$ and $\hat{\nu} = 1/2$). Such a case corresponds to that of zero-thickness cracks (see fig. 1 of Tsaur *et al.* 2011). Based on eqs (B7) or (B8), the crack-tip stress singularity is of order $r_1^{-1/2}$, which is commonly known in the field of fracture mechanics (e.g. Freund 1998).

APPENDIX C: ADDITIONAL REMARKS FOR EQ. (22)

When using the traditional RMT, the presence of singularities usually makes the construction of field solutions in the domains with non-smooth edges require a vast amount of eigenfunction expansions. Such a circumstance is analogous to the well-known Gibbs–Wilbraham phenomenon, that is, an issue regarding the slow convergence of the Fourier partial sums at a jump discontinuity. Gottlieb & Shu (1997) proposed the Fourier–Gegenbauer method (FGM) to entirely remove the Gibbs phenomenon. The core of the FGM hinges on the re-expansion of Fourier partial sums into the rapidly convergent Gegenbauer series. This solution concept allows one to deal with the problems involving singularities. Thus, the weighted Gegenbauer polynomials, that is,

$$(1 - \tilde{\sigma}^2)^{\xi - 1/2} C^{\xi}_{2m}(\tilde{\sigma}), \tag{C1}$$

provide a wide choice of basis functions because the weight function $(1 - \tilde{\sigma}^2)^{\xi - 1/2}$ can be adjusted flexibly to cover the expected singular behaviour. Evidently, if one attempts to explicitly model the dominant feature of singular stress fields around a right-angled corner, taking $\xi = 1/6$ in eq. (C1) gives an inverse cubic-root singularity. Furthermore, the form of the argument $\tilde{\sigma}$ depends only on the location of singular points. The reduction factor ψ_m is incorporated into the weighted Gegenbauer polynomials, so as to obtain a chain of concise results (eqs 24–26) after carrying out the integral transform shown in eq. (23).

Previous studies concerning the application of Gegenbauer polynomials to treat the corner singularities may trace back to those in the field of electromagnetics (e.g. Zargano *et al.* 1979).

APPENDIX D: EXPRESSIONS OF ASSOCIATED FUNCTIONS IN EQ. (39)

In eq. (39), the involved functions used for brevity are listed as follows:

$$U_{q,m} = \hat{U}^{(1)}_{q,m} + \hat{U}^{(2)}_{q,m} + \hat{U}^{(3)}_{q,m}, \tag{D1}$$

$$V_q = \hat{V}^{(1)}_q + \hat{V}^{(2)}_q, \tag{D2}$$

where

$$\hat{U}^{(1)}_{q,m} = \frac{1}{\pi} \sum_{n=0}^{\infty} \varepsilon_n \tilde{H}_{2n} J^{C1}_{m,n} J^{C1}_{q,n} + F_1, \tag{D3}$$

$$\hat{U}^{(2)}_{q,m} = -\frac{2}{\pi - \beta} \sum_{n=0}^{\infty} \varepsilon_n \tilde{J}_n J^{C2}_{m,n} J^{C2}_{q,n} + F_2, \tag{D4}$$

$$\hat{U}^{(3)}_{q,m} = \frac{2}{\pi} \sum_{n=0}^{\infty} \tilde{H}_{2n+1} J^{S}_{m,n} J^{S}_{q,n} + F_3, \tag{D5}$$

$$\hat{V}^{(1)}_q = \frac{4\mathrm{i}}{\pi a} \sum_{n=0}^{\infty} \frac{\varepsilon_n (-1)^n \cos(2n)\alpha}{H^{(2)\prime}_{2n}(ka)} J^{C1}_{q,n}, \tag{D6}$$

$$\hat{V}^{(2)}_q = \frac{8}{\pi a} \sum_{n=0}^{\infty} \frac{(-1)^n \sin(2n+1)\alpha}{H^{(2)\,\prime}_{2n+1}(ka)} J^{S}_{q,n}, \tag{D7}$$

together with

$$\tilde{J}_n = \frac{J_{n\,\nu}(ka)}{J'_{n\,\nu}(ka)}, \tag{D8}$$

$$\tilde{H}_n = \frac{H^{(2)}_n(ka)}{H^{(2)\prime}_n(ka)}, \tag{D9}$$

$$J^{C1}_{m,n} = \begin{cases} \frac{6}{2^{1/3}\Gamma(1/6)} \delta_{m,0}, & n = 0 \\ (-1)^{m+n} \frac{J_{2m+1/6}[2n(\pi-\beta)]}{[4n(\pi-\beta)]^{1/6}}, & n \neq 0 \end{cases}, \tag{D10}$$

$$J^{C2}_{m,n} = \begin{cases} \frac{6}{2^{1/3}\Gamma(1/6)} \delta_{m,0}, & n = 0 \\ (-1)^{m} \frac{J_{2m+1/6}(n\pi)}{(2n\pi)^{1/6}}, & n \neq 0 \end{cases}, \tag{D11}$$

$$J^{S}_{m,n} = (-1)^{m+n} \frac{J_{2m+1/6}\,[(2n+1)(\pi-\beta)]}{[(4n+2)(\pi-\beta)]^{1/6}}. \tag{D12}$$

In eqs (D10) and (D11), $\delta_{m,0}$ is the Kronecker delta function. Besides, the Kummer's transformation (Abramowitz & Stegun 1972), involving some auxiliary series constructed via the asymptotic expressions of Bessel and Hankel functions for large arguments and orders, may be exploited to accelerate the convergence of the first series in eqs (D3)–(D5). Thus, the second terms in eqs (D3)–(D5) are given, respectively, as follows:

$$F_1 = \frac{2^{-8/3}\pi^{-2}a}{(\pi-\beta)^{4/3}} \left\{ \sum_{n=1}^{\infty} n^{-7/3} \left[\cos(2n)\beta - \sqrt{3}\sin(2n)\beta \right]^2 - \frac{(1 + \mathrm{i}\sqrt{3})\mathrm{Li}_{7/3}(e^{-4\mathrm{i}\beta}) + (1 - \mathrm{i}\sqrt{3})\mathrm{Li}_{7/3}(\mathrm{e}^{4\mathrm{i}\beta})}{2} + 2\zeta(7/3) \right\}, \tag{D13}$$

$$F_2 = -\frac{2^{-1/3}\pi^{-2}a}{(\pi-\beta)^{4/3}} \left\{ \sum_{n=0}^{\infty} \frac{\left[\cos(2n+1)\beta - \sqrt{3}\sin(2n+1)\beta \right]^2}{(2n+1)^{7/3}} - 2^{-10/3}\mathrm{e}^{-2\mathrm{i}\beta}(1 + i\sqrt{3})\Phi\left(\mathrm{e}^{-4\mathrm{i}\beta}, 7/3, 1/2\right) \right.$$

$$- 2^{-10/3}\mathrm{e}^{2\mathrm{i}\beta}(1 - i\sqrt{3})\Phi\left(\mathrm{e}^{4\mathrm{i}\beta}, 7/3, 1/2\right)$$

$$- (2^{-4/3} - 4)\zeta(7/3)\Bigg\}, \tag{D14}$$

$$F_3 = \frac{2^{-1/3}\pi^{-7/3}a}{\nu(\pi - \beta)}\left[\sum_{n=1}^{\infty} n^{-7/3} - \zeta(7/3)\right], \tag{D15}$$

where $\mathrm{Li}_n(\cdot)$ is the polylogarithm, $\zeta(\cdot)$ is the Riemann zeta function and $\Phi(\cdot)$ is the Lerch transcendent.

APPENDIX E: SERIES SOLUTION DERIVED BY THE RMT

The series solution derived by the RMT is given herein. Using eq. (3) and multiplying the stress continuity condition (eq. 11) by cosine/sine functions, the following relations are obtained.

$$A_n = \frac{\varepsilon_n}{\pi}\sum_{p=0}^{\infty} C_p I^{CC}_{p,n}, \tag{E1}$$

$$B_n = \frac{2}{\pi}\sum_{p=0}^{\infty} C_p I^{CS}_{p,n}, \tag{E2}$$

where the functions $I^{CC}_{p,n}$ and $I^{CS}_{p,n}$ are given by

$$I^{CC}_{p,n} = \begin{cases} \pi - \beta, \, p = n = 0 \\ \frac{4n(\pi-\beta)(-1)^n}{8n} + \frac{\sin[n(3\pi-4\beta)]}{8n}, \quad p\nu = 2n \neq 0 \\ \frac{2n\cos[p\nu(\pi-\beta)]\sin[n(\pi-2\beta)]}{4n^2-(p\nu)^2} \\ -\frac{p\nu\cos[n(\pi-2\beta)]\sin[p\nu(\pi-\beta)]}{4n^2-(p\nu)^2}, \quad p\nu \neq 2n \end{cases}, \tag{E3}$$

$$I^{CS}_{p,n} = \begin{cases} \frac{2(2n+1)(\pi-\beta)(-1)^n}{4(2n+1)} + \frac{\sin[n(3\pi-4\beta)-2\beta]}{4(2n+1)}, \quad p\nu = 2n+1 \\ -\frac{(2n+1)\cos[p\nu(\pi-\beta)]\sin[n(\pi-2\beta)-\beta]}{(2n+1)^2-(p\nu)^2} \\ +\frac{p\nu\cos[n(\pi-2\beta)-\beta]\sin[p\nu(\pi-\beta)]}{(2n+1)^2-(p\nu)^2}, \quad p\nu \neq 2n+1 \end{cases}. \tag{E4}$$

Next, applying eqs (9) and (10) to the displacement continuity condition (eq. 37), and employing eqs (E1) and (E2) to eliminate the scattering coefficients A_n and B_n yields the following system of linear algebraic equations pertinent to the unknown coefficients C_n.

$$\sum_{n=0}^{\infty} C_n G_{q,n} = W_q, \qquad q = 0, 1, \ldots, \tag{E5}$$

in which

$$G_{q,n} = \frac{1}{\pi}\sum_{m=0}^{\infty}\varepsilon_m \tilde{H}_{2m} I^{CC}_{n,m} I^{CC}_{q,m} + \frac{2}{\pi}\sum_{m=0}^{\infty}\tilde{H}_{2m+1} I^{CS}_{n,m} I^{CS}_{q,m} - \delta_{n,q}\frac{\pi-\beta}{\varepsilon_q}\tilde{J}_q, \tag{E6}$$

$$W_q = \frac{4\mathrm{i}}{\pi a}\sum_{n=0}^{\infty}\frac{\varepsilon_n(-1)^n\cos(2n)\alpha}{H^{(2)\prime}_{2n}(ka)} I^{CC}_{q,n} + \frac{8}{\pi a}\sum_{n=0}^{\infty}\frac{(-1)^n\sin(2n+1)\alpha}{H^{(2)\prime}_{2n+1}(ka)} I^{CS}_{q,n}. \tag{E7}$$

In eq. (E5), choosing a finite truncation of the infinite series is required. The weighting indices q and the infinite sums with indices n and m are truncated after $M - 1$ terms. Consequently, a system of M equations with M unknowns can be solved by standard matrix techniques. Once the coefficients C_n are found, the scattering coefficients A_n and B_n can be straightforwardly evaluated via eqs (E1) and (E2).